

STUDY ON THE CORROSION RESISTANCE OF HOMOGENEOUS Mg-1Bi-0.5x (x=Nd,Ce,La) ALLOYS

ŠTUDIJA KOROZIJSKE ODPORNOSTI HOMOGENIH ZLITIN TIPA Mg-1Bi-0,5x (x=Nd,Ce,La)

Sichao Du¹, Zheng Jia^{1,2*}, Zhiwen Mao¹, Xiaowei Niu²

¹College of Mechanical Engineering, Shenyang University, Shenyang 110044

²College of Environment, Liaoning Province Environmental Pollution Remediation Professional Technology Innovation Center & Shenyang Key Laboratory of Collaborative Technology Innovation for Industrial Pollution Reduction and Carbon Reduction, Shenyang University, Shenyang 110044, China

Prejem rokopisa – received: 2024-07-23; sprejem za objavo – accepted for publication: 2024-10-10

doi:10.17222/mit.2024.1255

Mg alloys are widely used in the aerospace and automotive industries, as well as in electronic products due to their low density and high specific strength. However, the poor corrosion resistance of Mg alloys limits their applications. Rare earth elements have been shown to improve the corrosion resistance of alloys. In this study, Mg-1Bi-0.5x (x = Nd, Ce, La) alloys were prepared by alloying with Bi, Nd, Ce, and La. The microstructure and corrosion behavior of Mg-1Bi-0.5x (x = Nd, Ce, La) alloys were investigated using X-ray diffraction (XRD), optical microscopy (OM), scanning electron microscopy (SEM), hydrogen evolution tests, weight loss experiments, and electrochemical measurements. The results indicate that the Mg-1Bi-0.5Nd alloy exhibits higher corrosion potentials and lower corrosion current densities, indicating superior corrosion resistance. This improvement is attributed to the formation of a more stable and uniform film of corrosion products, which prevents further corrosion and enhances corrosion resistance.

Keywords: rare earth elements, corrosion resistance, electrochemistry, corrosion product film

Zlitine na osnovi magnezija (Mg) se veliko uporabljajo v letalski in avtomobilski industriji, kot tudi v elektronskih izdelkih, ker imajo majhno gostoto in veliko specifično trdnost. Vendar pa njihova relativno slaba odpornost proti koroziji omejuje njihovo širšo uporabnost. V nekaterih raziskavah avtorji ugotavljajo, da dodatek redkozemeljskih elementov izboljšuje njihovo odpornost proti koroziji. V tem članku avtorji opisujejo študijo priprave in karakterizacijo zlitin tipa Mg-1Bi-0,5x (x=Nd, Ce, La) legiranih z Nd, Ce, in La. Mikrostrukturo in korozijsko odpornost izdelanih zlitin so analizirali s pomočjo rentgenske difrakcije (XRD), optične (OM) in vrstične elektronske mikroskopije (SEM), s testom razvoja vodika, z eksperimenti izgube na masi in elektro-kemijskimi meritvami. Rezultati študije so pokazali, da ima zlitina Mg-1Bi-0,5Nd najboljšo odpornost proti koroziji, ker ima najvišji korozijski potencial in najnižjo korozijsko tokovno gostoto. Ta izboljšava je posledica tvorbe bolj stabilne in enovite tanke plasti korozijskega produkta na površini zlitine, ki preprečuje nadaljnjo korozijo zlitine.

Ključne besede:redkozemeljski elementi, odpornost proti koroziji, elektrokemija, tanka plast (film) nastalega korozijskega produkta

1 INTRODUCTION

In today's rapidly developing world, environmental pollution and energy crises have become urgent problems to solve. Mg alloys have become important materials in the aerospace and automobile industries, as well as in electronic products, due to their low density, high specific strength, and excellent thermal conductivity, promoting green development and harmonious coexistence between humans and nature. However, the poor corrosion resistance of Mg alloys significantly limits their promotion and application in corrosive environments.^{1,2} In recent years, researchers have improved the corrosion resistance of Mg alloys through surface coating and friction stir processing.³⁻⁵ However, these processes are relatively complex and not favorable for a large-scale commercial production. Alloying is currently considered an

economical and effective method to improve the corrosion resistance of alloys.

Numerous studies have demonstrated that rare earth elements (RE) are effective alloying additions for improving the corrosion resistance of alloys.⁶ Rare earth elements can precipitate rare earth phases in alloys, enhance the alloy structure, and improve the corrosion resistance of Mg alloys by reducing the number of second phases and refining the grains. Ding et al. investigated the effect of Nd addition on Mg-6Zn-1Mn alloys and found that the Mg-6Zn-1Mn-0.6Nd alloy exhibited the best corrosion resistance and discharge properties.⁷ This improvement was attributed to Nd's effect on the grain refinement of the alloy. Li et al. examined the effect of Ce on the corrosion resistance of Mg₁₇Al₁₂ compounds.⁸ Their results showed that when the Ce content reached 0.5 w%, the corrosion resistance of the compounds was significantly improved due to the formation of dense corrosion product films. Azzeddine et al. investigated the effect of rare earth elements on the corrosion

*Corresponding author's e-mail:
jz140@163.com (Zheng Jia)

resistance of Mg binary alloys and found that a large number of Mg₁₂La phases existed along the grain boundaries of the Mg-1.43La alloy, acting as an anodic phase and leading to severe pitting corrosion.⁹ The addition of an appropriate amount of Bi can optimize the microstructure of the alloy, thus improving the corrosion resistance of Mg alloys. Wang et al. studied the effect of Bi addition on the microstructure of the AZ80 Mg alloy and found a significant grain refining effect when the amount of Bi was less than 1 %.¹⁰

Currently, there are few studies on the corrosion performance of Mg alloys with the combined addition of Bi and rare earth elements. To further investigate the corrosion mechanism in Mg alloys with rare earth elements, a new Mg-1Bi-0.5x (x = Nd, Ce, La) alloy was prepared in this study, and its corrosion resistance was systematically evaluated. The second phase distribution and corrosion morphology of different alloys were analyzed to explore the corrosion mechanism. The results of this study provide theoretical support for further application of rare-earth Mg alloys and provide new insights into the development of new corrosion-resistant Mg alloy materials.

2 MATERIALS AND METHODS

2.1 Preparation of alloys

The Mg-1Bi-0.5x (x = Nd, Ce, La) alloys were prepared using industrially pure Mg (99.9 w%), pure Bi (99.9 w%), and intermediate alloys Mg-25%Nd, Mg-30%Ce, and Mg-25%La. Before melting, the surfaces of the crucible and mold required for casting were cleaned to remove surface oxides and then preheated. An Mg ingot was added to the preheated crucible, and the temperature was raised to 760 °C to melt it completely. After maintaining the temperature at 750 °C, the slag was skimmed, and pure Bi as well as the intermediate alloys Mg-25%Nd, Mg-30%Ce, and Mg-25%La were added. A No.5 melting agent was sprinkled on the surface of the melt and stirred for 2–3 min until fully melted. After the temperature was lowered to 720 °C and held for 20 min, the melt was cast into ϕ 60 × 240 mm mild steel molds protected by a mixture of CO₂ and SF₆ (100:1). To eliminate compositional segregation of the as-cast alloys, the resulting ingots were placed in a

box-type resistor furnace at 400 °C for 12 h and then quenched in water for homogenization.

The composition of the as-cast alloy was analyzed using inductively coupled plasma spectrometry (ICP), and the results are presented in **Table 1**.

Table 1: Chemical compositions of the alloys

Alloys	Chemical compositions (w/%)				
	Mg	Bi	Nd	Ce	La
Mg-1Bi-0.5Nd	Bal.	0.83	0.45	–	–
Mg-1Bi-0.5Ce	Bal.	0.84	–	0.56	–
Mg-1Bi-0.5La	Bal.	0.70	–	–	0.48

2.2 Microstructure

Samples were taken from the homogenized ingots, and specimens with dimensions of (10 × 10 × 10) mm were obtained using a wire cutter. The sampling area is shown in **Figure 1**. The samples were sanded with 800#, 1000#, 2000#, 3000#, and 5000# SiC sandpaper and then analyzed with an X-ray diffraction (XRD) analyzer to determine the phase composition of the alloy. Metallographic specimens were also polished with SiC sandpaper up to 5000# and then polished with a polishing paste of 0.5 μ m coarseness until the surface was mirror-like and free of visible scratches. The specimens were then rinsed with anhydrous ethanol and dried with cold air. Corrosion was carried out using a 4 % HNO₃ etching solution (a mixture consisting of 4 mL of HNO₃ and 96 mL of C₂H₆O) for 5–10 seconds, and the surfaces of the specimens were rinsed with anhydrous ethanol and dried after corrosion was completed. The microstructure of the alloy was observed using a metallographic microscope. The average grain size was calculated through the intercept method, aided by Image-Pro Plus software. SEM specimens were prepared using the same preparation method. The morphology, size, and distribution of the second phase in the alloy were observed using a field emission scanning electron microscope (SEM) equipped with an energy dispersive spectrometer (EDS).

2.3 Immersion experiments

The obtained specimens were sanded with 800#, 1000#, 2000#, 3000#, and 5000# SiC sandpaper near the center to create a smooth and flat test surface, while the remaining areas were encapsulated with epoxy resin to avoid interference. Before the weight loss test, the specimens were cleaned and dried to ensure no residual material remained on the surface. At a constant temperature of 25 °C, the treated specimens were placed in a 3.5 w% NaCl solution for the experiments, during which the corrosion behavior of the materials was evaluated by monitoring the volume of hydrogen evolution and the change in the mass of the specimens. The hydrogen evolution corrosion rate, P_H, of the specimens was calculated using Equation (1), which reflects the relationship between the volume of hydrogen evolved from the specimens and the

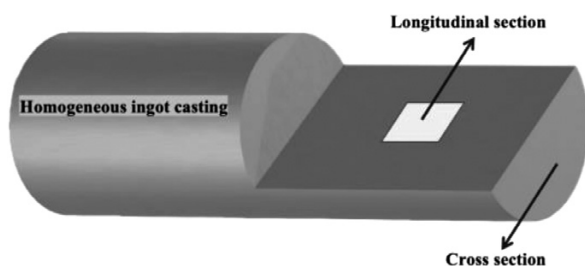


Figure 1: Specimen sampling location

corrosion rate. Equation (2) was used to calculate the weight loss corrosion rate, P_w , of the specimens.

$$P_H = \frac{8.76 \cdot 10^4 \cdot \Delta V \cdot M}{A \cdot t \cdot \rho} \quad (1)$$

$$P_w = \frac{8.76 \cdot 10^4 \cdot \Delta g}{A \cdot t \cdot \rho} \quad (2)$$

Here, P_H is the corrosion rate of the hydrogen precipitation test, $\text{mm} \cdot \text{year}^{-1}$; ΔV is the total amount of hydrogen precipitated during the hydrogen precipitation test, mL; M is the relationship between the rate of hydrogen production and the rate of alloy mass loss, with a value of 0.001083, $\text{g} \cdot \text{mL}^{-1}$; A is the exposed surface area of the alloy, cm^2 ; t is the immersion time, h; ρ is the density of the alloy, $\text{g} \cdot \text{cm}^{-3}$; and Δg is the mass loss of the alloy before and after immersion, g.

2.4 Electrochemical measurements

Electrochemical tests were conducted at room temperature using a standard three-electrode electrochemical workstation (CHI660E). The specimen of each test surface was first sequentially sanded with SiC sandpaper ranging from 400# to 5000# to ensure a smooth and flat surface. The back side of the test surface was connected by wires, and the remaining areas except the working surface were encapsulated with epoxy resin. The prepared working electrode was then immersed in a 3.5 w/% NaCl solution for 3600 s to achieve a stable open-circuit potential. The corrosion current density (i_{corr}) was obtained from the kinetic potential polarization curve measurements. The relationship between the corrosion current density and the corrosion rate was calculated using Equation (3).¹¹ Additionally, the electrochemical impedance spectroscopy data obtained from the tests were fitted and analyzed using Zsimpwin software. To ensure data reliability, three valid samples were tested for each alloy.

$$P_i = 22.85 \cdot i_{\text{corr}} \quad (3)$$

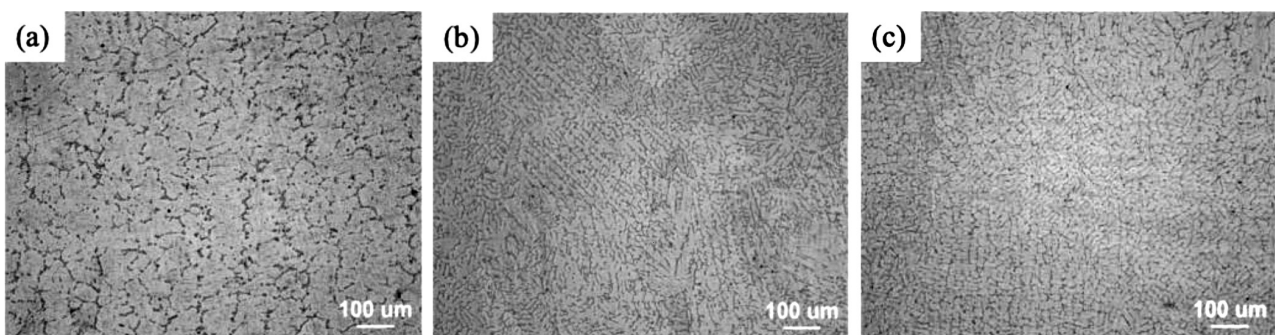


Figure 3: Metallographic structures: a) Mg-1Bi-0.5Nd, b) Mg-1Bi-0.5Ce, c) Mg-1Bi-0.5La

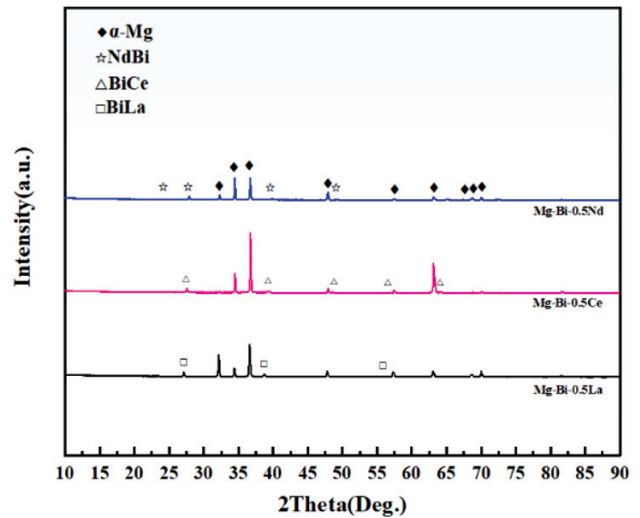


Figure 2: XRD patterns of homogeneous Mg-1Bi-0.5x (x = Nd, Ce, La) alloys

3 EXPERIMENTAL RESULTS AND DISCUSSION

3.1 Microstructure analysis

Figure 2 shows the XRD patterns of homogeneous Mg-1Bi-0.5x (x = Nd, Ce, La) alloys. The results indicate that the diffraction peaks of the homogeneous Mg-1Bi-0.5Nd alloy consisted of α -Mg and NdBi phases, while those of the Mg-1Bi-0.5Ce alloy comprised α -Mg and BiCe phases. Similarly, the diffraction peaks of the Mg-1Bi-0.5La alloy included α -Mg and BiLa phases. The formation of these phases was influenced by the electronegativity differences between the elements, which affected the ease of compound formation.¹² The electronegativities of Mg, Bi, Nd, Ce, and La were 1.31, 1.9, 1.14, 1.12, and 1.10, respectively. Therefore, significant electronegativity differences between the rare earth elements and Bi facilitated the formation of Bi-RE phases.

Figure 3 shows the metallographic structures of the three homogeneous state alloys. All three homogeneous alloys consisted of coarse dendrites, with the second phase precipitating at the grain boundaries. The addition of the Nd element reduced the amount of the second

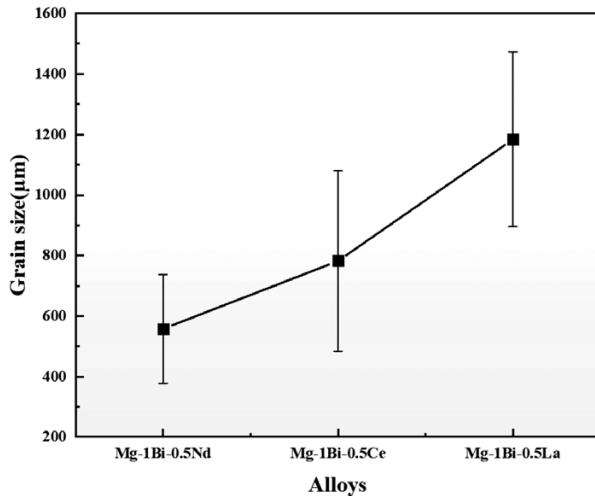


Figure 4: Grain size of the three alloys

phase in the alloy. A polarized light structure was used to measure the grain size of the alloys, as shown in **Figure 4**. All three alloys exhibited coarse grains, with Mg-1Bi-0.5Nd having a relatively smaller grain size. **Figure 5** shows SEM images of the three alloys, where the second phase area fractions were quantified using Image-Pro Plus software. It was found that Mg-1Bi-0.5Nd had the smallest second phase area frac-

tion of 1.3 %, while the second phase fractions of Mg-1Bi-0.5Ce and Mg-1Bi-0.5La were 3.3 % and 4.6 %, respectively. The second phases in Mg-1Bi-0.5Ce and Mg-1Bi-0.5La were reticulated, whereas the second phase in the Mg-1Bi-0.5Nd alloy was diffusely distributed in the form of strips. The three alloys displayed lumpy phases and strips of varying sizes. The second phases were analyzed with EDS, and the results are presented in **Table 2**. The striped phase at point A and the polygonal massive phase at point B contained large amounts of Nd and Bi elements, with an atomic ratio close to 1:1. This phase was identified as the NdBi phase, consistent with the XRD results. EDS analysis of points C, D, E, and F detected the enrichment of Bi and rare earth elements, with atomic ratios also close to 1:1, which, combined with the XRD data, allowed the determination of the BiCe phase and BiLa phase.

3.2 Corrosion performance

Figure 6 illustrates the average hydrogen precipitation volume and the average hydrogen precipitation weight loss corrosion rate for the three homogeneous alloys after immersion for 24 h. The Mg-1Bi-0.5Nd alloy exhibited the lowest corrosion rate compared to the other two alloys. **Figure 6a** demonstrated that the hydrogen

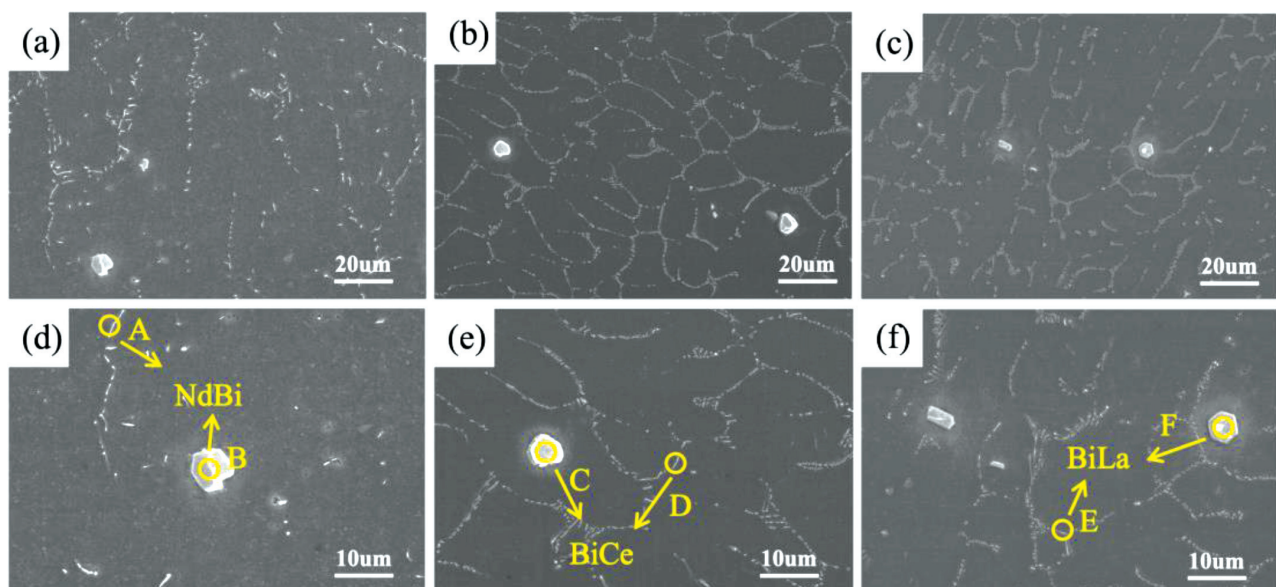


Figure 5: SEM images of the three alloys: a), d) Mg-1Bi-0.5Nd, b), e) Mg-1Bi-0.5Ce, c), f) Mg-1Bi-0.5La

Table 2: EDS analysis results

Point	Chemical composition ($\phi/\%$)					Phase types
	Mg	Bi	Nd	Ce	La	
A	74.14	13.02	12.84	–	–	NdBi
B	23.29	39.84	36.86	–	–	NdBi
C	95.38	2.48	–	2.15	–	BiCe
D	22.97	39.75	–	37.27	–	BiCe
E	94.08	3.01	–	–	2.91	BiLa
F	23.63	38.86	–	–	37.51	BiLa

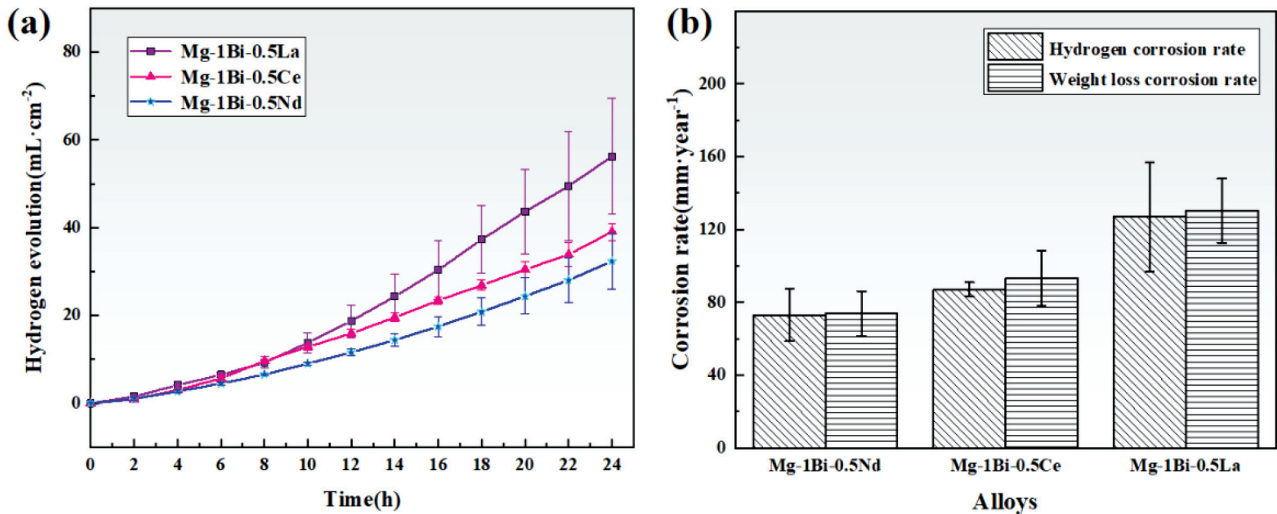


Figure 6: a) 24 h hydrogen precipitation volume, b) average hydrogen precipitation corrosion rate and average weight loss corrosion rate

precipitation reaction in the alloy occurred in two stages. Initially, during the first 2 h, the amount of hydrogen precipitated was low, and the corrosion rate was correspondingly lower. As shown in **Figure 7**, the macroscopic morphology after the removal of corrosion products revealed that the surfaces of the three alloys, immediately after immersion in the solution, were relatively smooth. At this stage, the corrosion process was relatively slow, with only localized pitting corrosion beginning to occur, resulting in a low corrosion rate. The slope for the Mg-1Bi-0.5La alloy in **Figure 6a** increased sharply after 8 h, indicating a significant rise in the corrosion rate at that point.

Figure 7i shows that deep corrosion pits formed locally, accompanied by the generation of black oxides, suggesting that the protective effect of the corrosion product film became limited and could not effectively protect the Mg matrix. Throughout the entire corrosion process, the slopes of the hydrogen precipitation curves for Mg-1Bi-0.5Nd and Mg-1Bi-0.5Ce alloys remained relatively stable, which was attributed to the dynamic equilibrium between the formation and shedding of the corrosion product film. After 24 h of corrosion, the corrosion pits on the surface of the Mg-1Bi-0.5Nd alloy were shallow, whereas more corrosion pits and black oxides appeared on the surface of the Mg-1Bi-0.5La alloy. The average hydrogen precipitation corrosion rate of the alloys was calculated using Equation (1), as shown in **Figure 6b**. The Mg-1Bi-0.5Nd alloy had the lowest hydrogen precipitation corrosion rate at 73.02 mm·year⁻¹. The average weight loss rate of the three alloys, calculated using Equation (2), was consistent with the hydrogen precipitation corrosion rate, with the Mg-1Bi-0.5Nd alloy exhibiting the lowest weight loss corrosion rate of 73.74 mm·year⁻¹.

Since Mg is an intrinsically passive element, pitting corrosion occurred in Mg alloys when exposed to Cl⁻ in the 3.5 w/% NaCl solution. It was demonstrated that the

second phase of the alloy and the Mg matrix formed a microcell, leading to micro-galvanic corrosion due to the potential difference between the second phase and the Mg matrix.¹³ The Mg matrix, which typically had a lower potential, acted as the anode, while the second phase with a higher potential served as the cathode, accelerating the corrosion of the Mg matrix. Consequently, the corrosion of Mg alloys was related to the distribution of the second phase within the alloys. The Mg-1Bi-0.5Nd alloy, having a smaller second phase area fraction, experienced a reduced rate of micro-galvanic

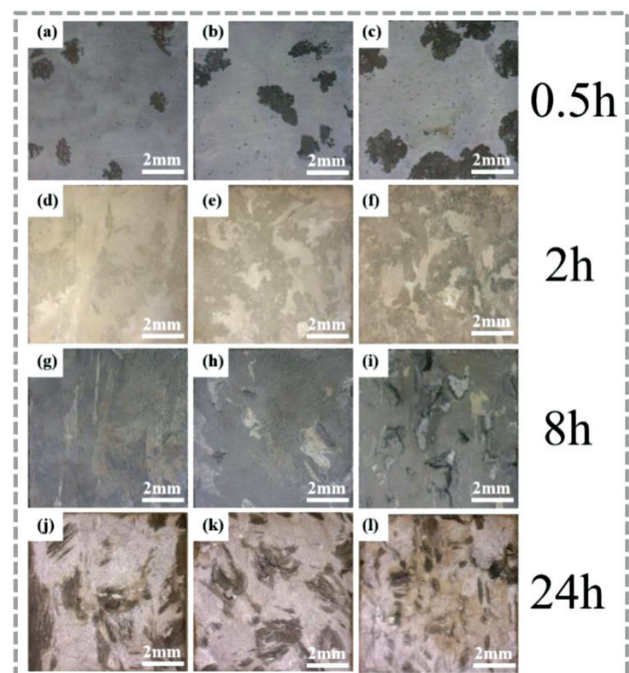


Figure 7: Macroscopic corrosion morphology of three alloys: a), d), g), j) Mg-1Bi-0.5Nd, b), e), h), k) Mg-1Bi-0.5Ce, c), f), i), l) Mg-1Bi-0.5La

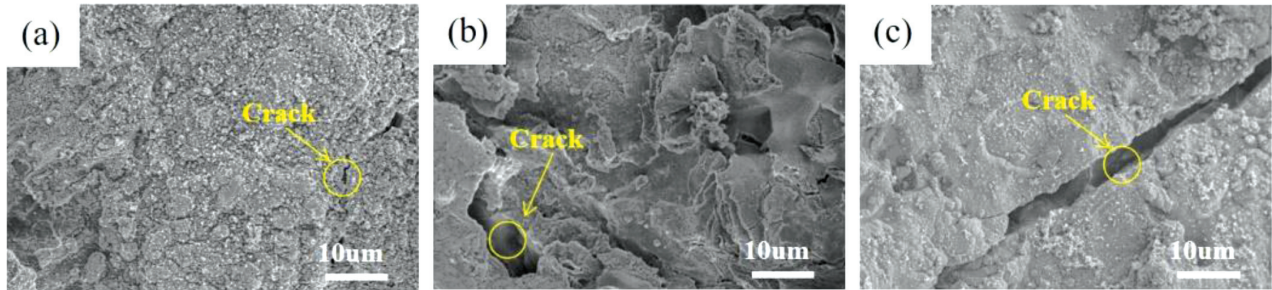


Figure 8: SEM pictures of the three alloys after 24h immersion without removing the surface corrosion products: a) Mg-1Bi-0.5Nd; b) Mg-1Bi-0.5Ce; (c) Mg-1Bi-0.5La

corrosion, leading to improved corrosion resistance compared to Mg-1Bi-0.5Ce and Mg-1Bi-0.5La alloys.

The characteristics of corrosion product films, such as their level of porosity, influenced the corrosion resistance of the alloys in various ways. The formation of the corrosion product film was related not only to the corrosion solution but also to the microstructure and other characteristics of the alloy. The effect of microstructure on the formation of the corrosion product film was complex. For Mg alloys, the grain boundaries exhibited a high chemical activity and energy. Therefore, a high grain boundary density in fine-crystalline materials could increase surface activity and rapidly form a passivation protective film.¹⁴ The high grain boundary density in fine-crystalline Mg alloys compensated for the mismatch between the oxides and the metal, promoting the formation of a denser and more uniform corrosion product film

on the surface, thereby improving corrosion resistance. In this study, the coarse dendritic structure led to a corrosion product film that could not adequately match the alloy in a timely manner, resulting in a product film with a limited protective effect. It was shown that grain refinement promoted the generation of a semi-protective anodic layer and improved the micro-galvanic corrosion behavior of Mg alloys.¹⁵ The $\text{Mg}(\text{OH})_2$ film formed during corrosion at grain boundaries, where chemical activity was higher, and the relatively fine grain size of the Mg-1Bi-0.5Nd alloy facilitated the formation of a more effective corrosion product film, giving it the best corrosion resistance among the three alloys.

Figure 8 shows SEM images of the corrosion product films produced by the alloys in the 3.5 w/% NaCl solution after 24 h of immersion. The corrosion product film on the Mg-1Bi-0.5Nd alloy was distributed in spher-

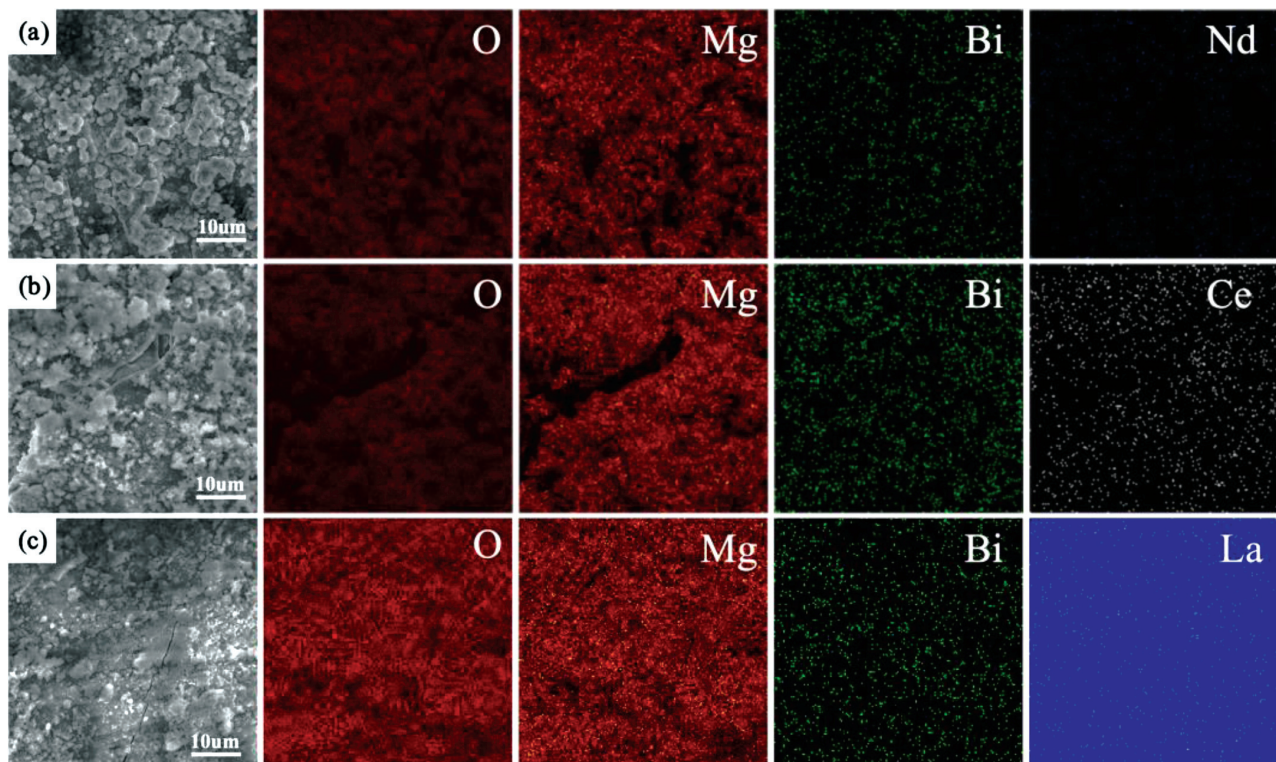


Figure 9: SEM/EDS images of corrosion products on the surfaces of three alloys: a) Mg-1Bi-0.5Nd, b) Mg-1Bi-0.5Ce, c) Mg-1Bi-0.5La

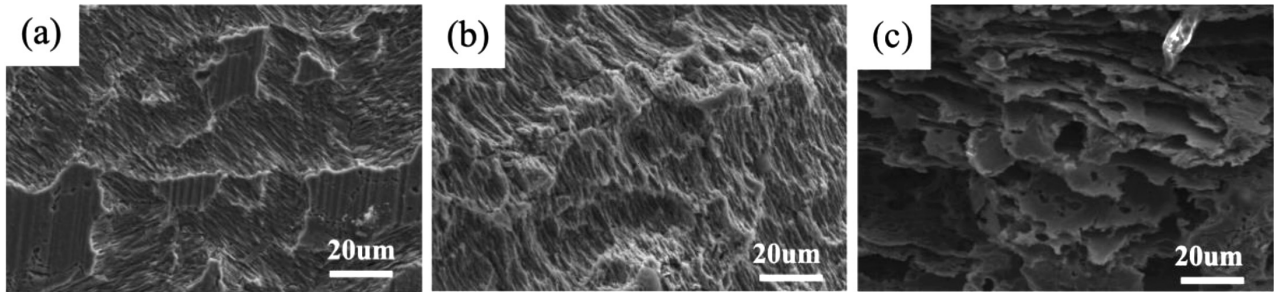


Figure 10: SEM images of three alloys after the removal of surface corrosion products after 24 h immersion: a) Mg-1Bi-0.5Nd, b) Mg-1Bi-0.5Ce, c) Mg-1Bi-0.5La

ical shapes over the surface of the Mg matrix, covering the alloy and providing a relatively dense film that partially prevented the alloy from reacting with the solution, thus slowing down its corrosion. The corrosion product film of the Mg-1Bi-0.5Ce alloy consisted of layers of flakes covering the surface, with numerous pores between the flakes. This relatively loose surface film had a limited protective effect and was insufficient to prevent the alloy corrosion. The corrosion product film of the Mg-1Bi-0.5La alloy exhibited a diffuse distribution of spherical shapes and did not adequately cover the alloy surface. **Figure 8c** shows corrosion cracks and the bare metal surface of the alloy. The surface scanning results of the corrosion product film, shown in **Figure 9**, indicated that the product film was primarily composed of Mg and O elements, with a small amount of Bi and rare earth elements enriched. This suggested that the product film was mainly $\text{Mg}(\text{OH})_2$, which was consistent with the previous studies reporting that the corrosion products of Mg alloys are predominantly $\text{Mg}(\text{OH})_2$.¹⁶

Figure 10 illustrates the SEM analysis of the alloy surfaces after removing the corrosion products. The corrosion pits on the surface of the Mg-1Bi-0.5La alloy were deeper and they varied in depth, with severe laminar corrosion occurring locally. This loose laminar morphology increased the contact area between the alloy surface and the solution, which further promoted the hydrogen precipitation reaction. In contrast, the corro-

sion pits on the surface of the Mg-1Bi-0.5Ce alloy were more uniform and shallower, but the smooth and flat metal surface was no longer visible. The non-lamellar surface morphology relatively reduced the contact area between the alloy and the solution, thereby slowing down the hydrogen precipitation reaction. The surface of the Mg-1Bi-0.5Nd alloy remained smooth and flat with a significantly reduced corrosion area. Better surface quality implied a lower mass transfer of the alloy in the corrosive solution, indicating that superior surface quality corresponded to better corrosion resistance.¹⁷ The corrosion resistance of the alloys, assessed on the basis of corrosion morphology, was ranked as $\text{Mg-1Bi-0.5Nd} > \text{Mg-1Bi-0.5Ce} > \text{Mg-1Bi-0.5La}$, which aligned with the results of the hydrogen evolution experiment.

Based on the above results, corrosion mechanism diagrams for the three alloys are shown in **Figure 11**. In the early stage of corrosion, the alloys exhibited localized corrosion. The second phase formed micro-galvanic cells with the Mg matrix, and the resultant Mg^{2+} reacted with OH^- in the solution to form $\text{Mg}(\text{OH})_2$, which effectively protected the α -Mg matrix during this initial stage. However, over time, Cl^- ions further eroded the protective $\text{Mg}(\text{OH})_2$ film. Additionally, the coarse grain size of the Mg-1Bi-0.5La alloy caused a mismatch between the corrosion product film and the metal, which led to the deepening of the corrosion.

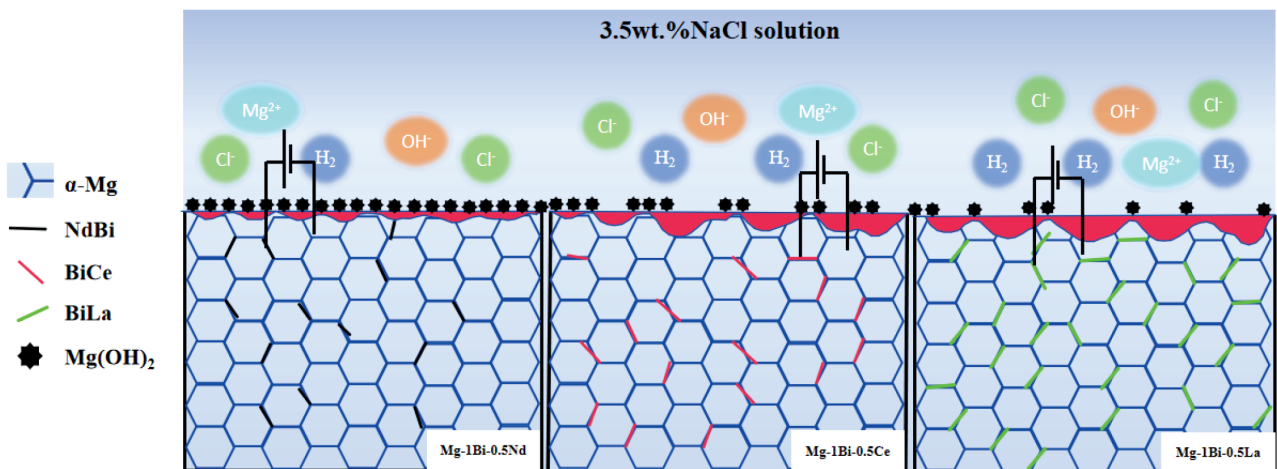


Figure 11: Corrosion mechanism diagram for the three alloys

3.3 Electrochemical performance

Figure 12 shows dynamic potential polarization curves of the three alloys in the 3.5 w/% NaCl solution. The cathodic branch of the polarization curves corresponded to the hydrogen precipitation reaction, while the anodic branch corresponded to the dissolution reaction of the α -Mg matrix. The cathodic region of the polarization curves displayed a stable linear region, indicating that the alloys maintained a consistent corrosion rate throughout the corrosion process. The self-corrosion potentials (E_{corr}) and self-corrosion current densities (i_{corr}) of the alloys, determined by fitting the polarization curves, are presented in Table 3. The open-circuit potential was defined as the steady-state self-corrosion potential of the alloy in the absence of an applied current. The corrosion potential is a thermodynamic parameter, and a more negative steady-state self-corrosion potential generally indicated a greater tendency of an alloy to corrode, but it could not be used to determine the corrosion resistance. The key factor for assessing the corrosion resistance of an alloy was the corrosion current density; a lower corrosion current density indicated a lower corrosion rate. According to Equation (3), the Mg-1Bi-0.5Nd alloy had the smallest corrosion current density of 27.03 $\mu\text{A}\cdot\text{cm}^{-2}$, indicating the best corrosion resistance, which was consistent with the results of the hydrogen evolution experiment.

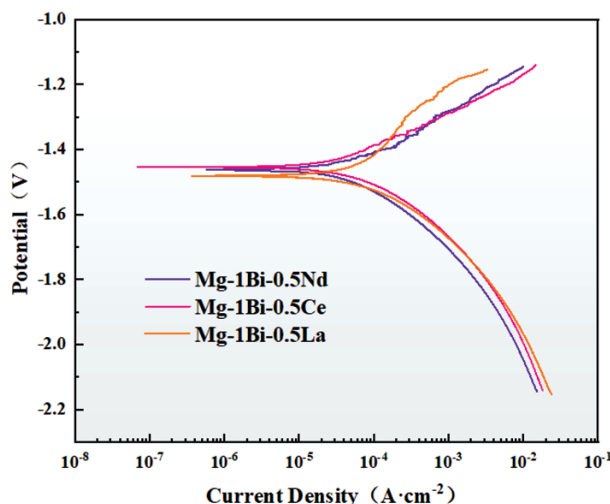


Figure 12: Polarization curves

Table 3: Corrosion parameters from polarization curves of the as-extruded alloys in 3.5 w/% NaCl solution

Alloy	E_{corr} (V)	i_{corr} ($\mu\text{A}\cdot\text{cm}^{-2}$)	P_i (mm·year ⁻¹)
Mg-1Bi-0.5Nd	-1.46	27.03	0.62
Mg-1Bi-0.5Ce	-1.45	37.03	0.85
Mg-1Bi-0.5La	-1.48	50.80	1.16

Figure 13 presents the Nyquist plots, Bode phase angle plots, impedance mode plots, and equivalent circuit

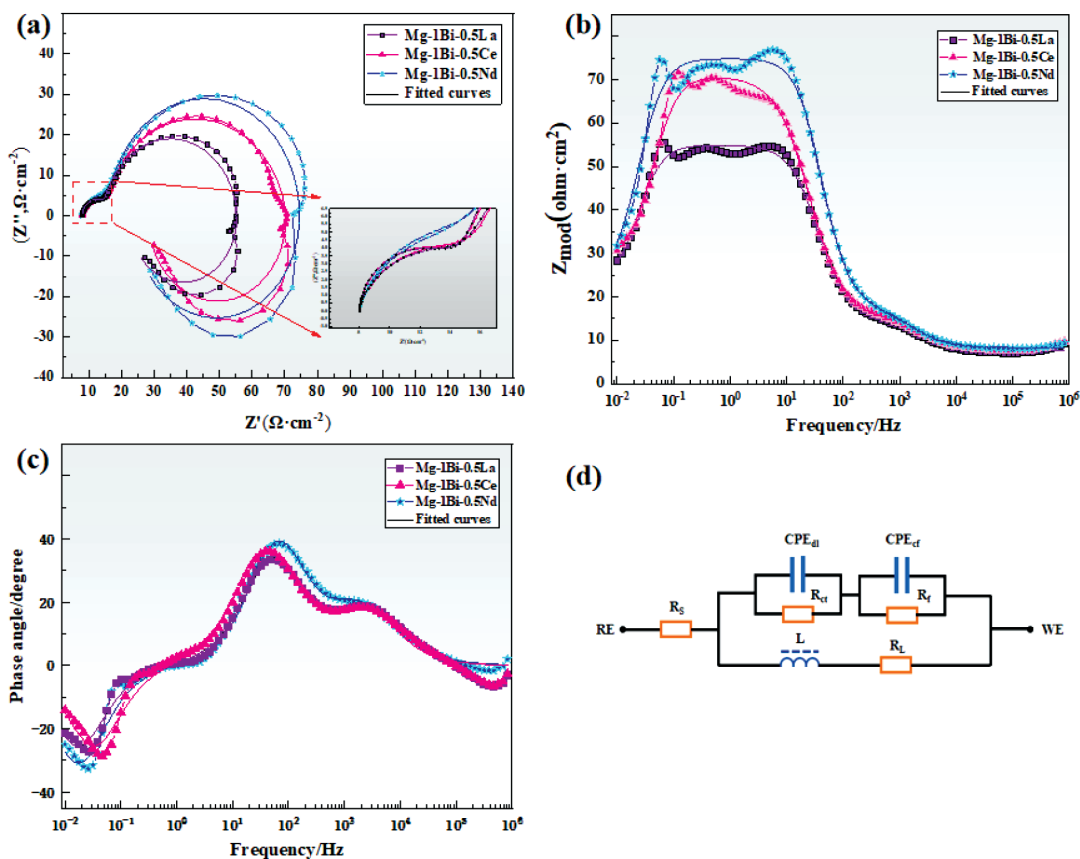


Figure 13: EIS plots of the three alloys: a) Nyquist plots, b) Bode phase angle plots, c) impedance modes plots, d) equivalent circuit diagram

Table 4: Fitting results for the EIS measurement of the three alloys in 3.5 w/% NaCl solution

Alloy	R_s	CPE_{dl}		R_{ct}	CPE_f		R_f	R_L	L
	$\Omega \cdot \text{cm}^2$	$Y_1/\mu\Omega^{-1} \cdot \text{cm}^{-2}$	n_1	$\Omega \cdot \text{cm}^2$	$Y_2/\mu\Omega^{-1} \cdot \text{cm}^{-2}$	n_2	$\Omega \cdot \text{cm}^2$	$\Omega \cdot \text{cm}^2$	$\text{H} \cdot \text{cm}^2$
Mg-1Bi-0.5Nd	8.267	89.6	0.99	57.35	51.48	0.85	9.16	20.73	452.2
Mg-1Bi-0.5Ce	8.074	248.6	0.89	56.27	17.17	0.96	6.65	29.69	280.7
Mg-1Bi-0.5La	7.526	15.81	0.96	47.44	116.5	0.95	9.927	20.58	390.6

diagram of the alloys, illustrating the electrochemical impedance behavior of the three different alloys at a stable open-circuit potential in the 3.5 w/% NaCl solution. From the Nyquist curves in **Figure 13a**, it was observed that all three alloys exhibited high-frequency capacitance arcs, medium-frequency capacitance arcs, and low-frequency susceptibility arcs, suggesting that the corrosion mechanism of the three alloys remained unchanged. The Bode plots confirmed the results of the Nyquist plots, while the size and diameter of the capacitance arcs varied significantly among the alloys, indicating different corrosion rates. Generally, the capacitance arc in the high-frequency region was related to the charge transfer in the double electric layer between the alloy surface and the electrolyte surface.¹⁹ The Mg-1Bi-0.5Nd alloy had the largest high-frequency capacitance arc, which provided significant resistance to the charge transfer during the corrosion process, thus protecting the α -Mg matrix to some extent.

Srinivasan et al. reported that the presence of a low-frequency inductance profile indicated an electrolyte diffusion between the material interface and the product film, leading to localized corrosion, as also depicted in **Figure 7**.²⁰ The Bode phase angle plot in **Figure 13b** shows a distinct wave peak in the high-frequency region, with the Mg-1Bi-0.5Nd alloy having the largest peak and peak width. The impedance mode plot in **Figure 13c** shows that the Mg-1Bi-0.5Nd alloy exhibited the highest impedance modulus value ($|Z|$), consistent with the results of the Nyquist plot, indicating that the Mg-1Bi-0.5Nd alloy had the lowest corrosion rate.

It was reported that the reaction of Mg alloys typically involves the electrochemical reaction of Mg with H_2O to produce $\text{Mg}(\text{OH})_2$ and H_2 .²¹ Based on the Nyquist diagram and the overall corrosion reaction of the alloy in the 3.5 w/% NaCl solution, the equivalent electric circuit (EEC) is shown in **Figure 13d**, where the charge transfer resistance (R_{ct}), the electrolyte resistance (R_s), and the Mg matrix/film interface double layer capacitance (CPE_{dl}) were identified as the main parameters. Symbols R_f and CPE_f represent the film resistance and film capacitance, respectively. To account for the inductive behavior, inductance (L) and resistance (R_L) were introduced into the model of the alloy. The impedance data were fitted, and the results are listed in **Table 4**. The R_s values were nearly identical and relatively small due to the good conductivity of the NaCl solution. The R_{ct} value was used to determine the corrosion resistance of the alloys. In general, a larger R_{ct} value indicates better corrosion re-

sistance, and the R_{ct} value of the Mg-1Bi-0.5Nd alloy was significantly higher than that of the other two alloys, indicating high corrosion resistance. This was related to the protection of the Mg matrix by the corrosion product film, and the addition of 0.5 % Nd produced a denser oxide film compared to the other two elements, which hindered electron transfer.

4 CONCLUSIONS

(1) The second phase types of the three alloys were altered: the Mg-1Bi-0.5Nd alloy formed the NdBi phase, the Mg-1Bi-0.5Ce alloy formed the BiCe phase, and the Mg-1Bi-0.5La alloy formed the BiLa phase. All three alloys consisted of coarse dendrites, and the Mg-1Bi-0.5Nd alloy had a relatively small grain size.

(2) The corrosion resistance of the alloys was characterized with hydrogen precipitation weight loss experiments, and the Mg-1Bi-0.5Nd alloy exhibited the lowest hydrogen precipitation corrosion rate of 73.02 mm-year⁻¹. This was attributed to the formation of a denser corrosion product film during corrosion, which protected the alloy and reduced the erosion due to the solution. The lower area fraction of the second phase also decreased the micro-galvanic corrosion to some extent.

(3) Fitting the polarization curves revealed that the Mg-1Bi-0.5Nd alloy had the smallest corrosion current density, i_{corr} , indicating that its corrosion resistance was the best among the three alloys. The results of the EIS experiments indicated that the additions of different elements did not alter the corrosion mechanism of the three alloys; however, the Mg-1Bi-0.5Nd alloy exhibited the highest corrosion resistance.

Acknowledgements

The authors acknowledge the financial support from the Liaoning Province Natural Science Foundation Project of China (2023-MS-321) and the Liaoning Province International Cooperation Project (Project Number: 2023030491-JH2/107).

5 References

- Y. H. Sun, F. Zhang, R. C. Wang, C. Q. Peng, J. R. Ren, Improving the corrosion resistance of Mg-8Li-3Al-2Zn alloy by combining Gd alloying and hot extrusion, *J. Alloys Compd.*, 964 (2023), 171205, doi:10.1016/j.jallcom.2023.171205
- J. Y. Yin, M. Li, F. Y. Yi, X. J. Zhao, D. K. Guan, K. C. Wang, Y. H. Gao, C. M. Liu, Effects of micro-alloying Ag on microstructure, me-

- chanical properties and corrosion behavior of extruded Mg-2Zn-0.2Ca-xAg alloys, *J. Alloys Compd.*, 989 (2024), 174376, doi:10.1016/j.jallcom.2024.174376
- ³ Z. Gruba, I. Škugor Rončević, M. Metikoš-Huković, Corrosion properties of the Mg alloy coated with polypyrrole films, *Corros. Sci.*, 102 (2016), 310–316, doi:10.1016/j.corsci.2015.10.022
- ⁴ A. Kania, W. Pilarczyk, M. M. Szindler, Structure and corrosion behavior of TiO₂ thin films deposited onto Mg-based alloy using magnetron sputtering and sol-gel, *Thin Solid Films*, 701 (2020), 137945, doi:10.1016/j.tsf.2020.137945
- ⁵ B. M. Hasani, H. Hedaiatmofidi, A. Zarebidaki, Effect of friction stir process on the microstructure and corrosion behavior of AZ91 Mg alloy, *Mater. Chem. Phys.*, 267 (2021), 124672, doi:10.1016/j.matchemphys.2021.124672
- ⁶ J. X. Niu, Q. R. Chen, N. X. Xu, Z. L. Wei, Effect of combinative addition of strontium and rare earth elements on corrosion resistance of AZ91D Mg alloy, *Trans. Nonferrous Met. Soc. China*, 18 (2008) 5, 1058–1064, doi:10.1016/S1003-6326(08)60181-8
- ⁷ D. Y. Ding, Y. H. Du, M. F. Tang, B. Song, N. Guo, H. J. Zhang, S. F. Guo, Corrosion and discharge behavior of Mg-Zn-Mn-Nd alloys as primary Mg-air batteries anode, *Trans. Nonferrous Met. Soc. China*, 33 (2023) 7, 2014–2029, doi:10.1016/S1003-6326(23)66240-5
- ⁸ A. R. Li, Z. Wu, J. L. Wei, P. P. Wu, Y. Z. Zhang, H. J. Wu, S. S. Liang, H. Yong, G. L. Song, D. Q. Fang, B. S. Liu, Y. H. Wei, Enhanced corrosion resistance of Mg₁₇Al₁₂ compounds by Ce modification, 218 (2023), 112663, doi:10.1016/j.vacuum.2023.112663
- ⁹ H. Azzeddine, A. Hanna, A. Dakhouche, L. Rabahi, N. Scharnagl, M. Dopita, F. Brisset, A.-L. Helbert, T. Baudin, Impact of rare-earth elements on the corrosion performance of binary Mg alloys, *J. Alloys Compd.*, 829 (2020), 154569, doi:10.1016/j.jallcom.2020.154569
- ¹⁰ W. Y. Xiao, Z. J. Xue, Y. Y. Sheng, Effect of Bi addition on microstructures and mechanical properties of AZ80 Mg alloy, *Trans. Nonferrous Met. Soc. China*, 21 (2011) 4, 711–716, doi:10.1016/S1003-6326(11)60770-X
- ¹¹ Z. Shi, A. Atrens, An innovative specimen configuration for the study of Mg corrosion, *Corros. Sci.*, 53 (2011) 1, 226–246, doi:10.1016/j.corsci.2010.09.016
- ¹² A. K. Mukhopadhyay, Nucleation of Ω Phase in an Al-Cu-Mg Alloy Containing Small Additions of Ag, *Mater. Trans., JIM*, 38 (1997) 5, 478–482, doi:10.2320/matertrans1989.38.478
- ¹³ A. E. Coy, F. Viejo, P. Skeldon, G. E. Thompson, Susceptibility of rare-earth-Mg alloys to micro-galvanic corrosion, *Corros. Sci.*, 52 (2010) 12, 3896–3906, doi:10.1016/j.corsci.2010.08.006
- ¹⁴ K. D. Ralston, N. Birbilis, Effect of Grain Size on Corrosion: A Review, *Corrosion*, 66 (2010) 7, 075005–075005-13, doi:10.5006/1.3462912
- ¹⁵ G. R. Argade, S. K. Panigrahi, R. S. Mishra, Effects of grain size on the corrosion resistance of wrought Mg alloys containing neodymium, *Corros. Sci.*, 58 (2012), 145–151, doi:10.1016/j.corsci.2012.01.021
- ¹⁶ I. Marco, O. Biest, Polarization measurements from a rotating disc electrode for characterization of Mg corrosion, *Corros. Sci.*, 102 (2016), 384–393, doi:10.1016/j.corsci.2015.10.031
- ¹⁷ S. Banerjee, S. Poria, G. Sutradhar, P. Sahoo, Corrosion behavior of AZ31-WC nano-composites, *J. Magnesium Alloys*, 7 (2019) 4, 681–695, doi:10.1016/j.jma.2019.07.004
- ¹⁸ C. L. Zhang, F. Zhang, L. Song, R. C. Zeng, S. Q. Li, E. H. Han, Corrosion resistance of a superhydrophobic surface on micro-arc oxidation coated Mg-Li-Ca alloy, *J. Alloys Compd.*, 728 (2017) 25, 815–826, doi:10.1016/j.jallcom.2017.08.159
- ¹⁹ H. Seifiyan, M. H. Sohi, M. Ansari, D. Ahmadkhanhiha, M. Saremi, Influence of friction stir processing conditions on corrosion behavior of AZ31B Mg alloy, *J. Magnesium Alloys*, 7 (2019) 4, 605–616, doi:10.1016/j.jma.2019.11.004
- ²⁰ S. A. Srinivasan, K. S. Shin, N. Rajendran, Applications of dynamic electrochemical impedance spectroscopy (DEIS) to evaluate protective coatings formed on AZ31 Mg alloy, *RSC Adv.*, 5 (2015) 37, 29589–29593, doi:10.1039/C4RA16967K
- ²¹ S. Feliu, A. Samaniego, V. Barranco, A. A. El-Hadad, I. Llorente, C. Serra, J. C. Galván, A study on the relationships between corrosion properties and chemistry of thermally oxidised surface films formed on polished commercial Mg alloys AZ31 and AZ61, *Applied Surface Science*, 295 (2014), 219–230, doi:10.1016/j.apsusc.2014.01.033